Construction and Building Materials 274 (2021) 121898

Contents lists available at ScienceDirect

Construction and Building Materials

journal homepage: www.elsevier.com/locate/conbuildmat

Characterization of hydration and dry shrinkage behavior of cement emulsified asphalt composites using deep learning

Zheng Tong [a], Zhenjun Wang [b,*], Xiaofeng Wang [c], Yuwei Ma [d], Haoyan Guo [a], Cunqiang Liu [a]

[a] Research and Development Center of Transport Industry of Technologies, Materials and Equipment of Highway Construction and Maintenance, Lanzhou 730030, PR China
[b] Chang'an University, School of Materials Science and Engineering, Xi'an 710061, PR China
[c] Henan Provincial Communications Planning & Design Institute, Zhengzhou 450052, PR China
[d] Shihezi University, College of Water Conservancy and Architectural Engineering, Shihezi 832000, PR China

HIGHLIGHTS

- A deep-learning framework characterizes hydration of CEACs.
- A deep-learning framework characterizes dry shrinkage of CEACs.
- A deep-learning framework generates XRD spectrum and SEM images.

ARTICLE INFO

Article history:
Received 18 May 2020
Received in revised form 12 October 2020
Accepted 30 November 2020
Available online 30 December 2020

Keywords:
Cement emulsified asphalt composite
Ddry shrinkage
Hydration
Generative adversarial network
Deep neural network

ABSTRACT

This paper introduces a study of characterizing hydration and dry shrinkage behavior of cement emulsified asphalt composites (CEACs) through a deep-learning framework. The deep-learning framework consisted of two parts: generative adversarial networks (GANs) and deep neural networks (DNNs). The GAN part was first developed to map the design parameters of a CEAC to its X-ray powder diffraction (XRD) spectrum and scanning electron microscope (SEM) images. The DNN part was then designed to predict the dry shrinkage behavior of the CEAC based on its design parameters and the outputs of the GAN part. Finally, the effectiveness of the deep-learning framework was tested by 36 groups of CEACs. The results showed that the outputs of the GAN part, synthetic XRD spectrums and SEM images, were close to the measured data. Thus, the synthetic data were capable of characterizing the hydration processes and the microstructure of the CEACs. The DNN predicted the dry shrinkage ratios of the 36 groups with a 2.70% average error, demonstrating its high and stable precision. The feature vectors in the DNN provided a new method to characterize the effects of the design parameters on the dry shrinkage ratios. From the distribution of the feature vectors in a two-dimension space, we found that the curing time had the most significant effects on the dry shrinkage ratios, followed by the aggregate grading and the contents of cement and emulsified asphalt.

1. Introduction

Since the discovery of cement emulsified asphalt composites (CEACs), they have become an essential part of environment-friendly and multi-functional pavement materials [1–3]. However, the properties of CEACs are always uncertain due to their various material contents, internal structures, curing conditions, and so on. For example, a large number of experiment results indicated that the properties of CEACs were influenced by the contents of cement and emulsified asphalt [4,5], as well as solid volume fraction [6] and cement properties [7]. The deep understanding of curing conditions also demonstrated the effects of curing age and humidity on the properties of CEACs [8,9]. Condition variation during service, such as temperatures [10,11], also showed the effects on the properties of CEACs. Thus, novel approaches for the characterization and prediction of CEAC properties are needed to increase the rate at which new CEACs are designed and simultaneously decrease the associated cost of laboratory and field tests.

To date, there are many rule-based methods for the characterization and prediction of CEAC properties. For example, Fedrigo et al. [12] developed empirical formulas for predicting the shrinkage behaviors of cement-treated recycled pavement materials. Behnam et al. [13] proposed a new formulation to predict the

* Corresponding author.
E-mail address: zjwang@chd.edu.cn (Z. Wang).

https://doi.org/10.1016/j.conbuildmat.2020.121898
0950-0618/

compressive strength of preformed-foam cellular concrete. Tian et al. [14] built linear regression models between early-age strength and performance of CEACs. In addition, Ouyang et al. [15] measured the effects of wetting agent and superplasticizer on the fresh properties of CEACs. Similar studies can also be found in [16,17]. In general, the property prediction of CEACs using rule-based methods is usually limited by a range of input conditions. Thus, these predictions are generally extrapolative in practice. Moreover, the determination of empirical constants is not easy to obtain.

The past decades have seen success cases in the use of machine learning (and especially neural network) to characterize and predict material properties. For example, Wang et al. [18] proposed a neural network to predict the fatigue life of CEACs with acceptable precision. Yang et al. [19] predicted the mechanical properties of CEACs using neural networks and genetic algorithms. The reported maximum errors of the predicted shear and tension stresses were less than 6.28%. Zavrtanik et al. [20] used neural networks for modeling air void contents in asphalt mixtures, in which a large dataset with seven types of asphalt mixtures and ten design parameters was used for training the neural networks to achieve high-precise prediction. Moghaddam et al. [21] presented an application of support vector machines for the characterization of fatigue life of polyethylene terephthalate modified asphalt mixtures. Similar applications can also be found in some other studies [22–24]. However, to date, most research applying machine learning to the task is still infancy and has revolved around feature engineering. It means that humans provide some naive features (e.g., material components and contents) for a machine learning algorithm while it has been applied in a variety of situations. Thus, unacceptable errors always exist in the machine learning-based models since only a few of human-provided features are used for the characterization and prediction of material properties. Two reasons cause it. The first is that some features, which are not easily observed and measured, are neglected but should be considered in practice, such as hydration and microstructure. The second is that feature representation of CEACs depends on the subjective understanding of humans owing to a shortage of theoretical evidence, even though the mapping from these representations to properties is conducted autonomously. Thus, machine learning-based models have yet to become widely adopted.

This unsatisfactory situation of the use of machine learning for the characterization and prediction of material properties is reminiscent of the state of image-processing models before the broad adoption of deep learning. Deep learning, as a class of machine learning, uses multiple layers to extract higher-level features from the raw input progressively and maps these high-level features to targets [25,26]. It has achieved astonishing success in processing natural language [27], generating complex signals and images [28,29], and even discovering new antibiotics [30,31]. Two recent achievements make it possible that the success of deep learning can be duplicated in the case of characterization and prediction of material properties, especially CEAC properties:

- Historically, the large-scale studies about CEAC properties have generated data at an unprecedented rate, such as [20,32–34]. With these unaware data as a database, the time is ripe for applying more powerful and flexible machine learning models to the case mentioned above, such as deep learning.
- Some successful applications of deep learning in the field of material science demonstrate the feasibility of building a relationship between design parameters and material microstructure. For example, Liu et al. [35] proposed region-based deep learning models to characterize the dispersion of carbon bunches using scanning electron microscope (SEM) images. Tong et al. [36,37] proposed deep convolutional neural networks for evaluating carbon fiber morphology distribution and the predicting the properties of carbon fiber reinforced cement-based composites. Yuan et al. [38] predicted the electrical conductivity of cement-based composites using deep learning models. Additionally, Tong et al. [39] proposed a deep learning-based method to design fiber reinforced cement-based composites.

Motivated by the two achievements, this work aims to characterize hydration and dry shrinkage behavior of CEACs through a deep-learning framework. To be precise, the proposed framework is capable of mapping the design parameters of CEACs to their X-ray powder diffraction (XRD) spectrums and SEM images. The synthetic XRD spectrum and SEM images can characterize hydration and microstructure of CEACs. The model can also predict the dry shrinkage behavior of CEACs based on its learned features from the synthetic data and other information of CEACs. The remaining paper is organized as follows. Section 2 starts with the introduction of the proposed framework for CEAC property characterization. The experimental details of the use of the framework in the characterization of hydration and dry shrinkage behaviors of CEACs are presented in Section 3. In Section 4, we discuss the performance of the proposed framework. The conclusions of this work are summarized in Section 5.

2. Methodology

This chapter describes the proposed deep-learning framework in details. In Section 2.1, an overview of the framework is presented. In Section 2.2, generative adversarial networks are designed to characterize hydration and microstructure of CEACs. In Section 2.3, deep neural networks are introduced to predict the dry shrinkage behaviors of CEACs.

2.1. Overview

We developed a deep-learning framework to characterize the hydration, the microstructure, and the dry shrinkage behaviors of CEACs. Fig. 1 illustrates our model framework. The framework consisted of two parts: generative adversarial networks (GANs) and deep neural networks (DNNs).

For a CEAC with its design parameter set $\boldsymbol{x}$, the GAN part can be described as a function $G(\boldsymbol{x}_1,\boldsymbol{z}) \rightarrow \boldsymbol{y}$, where $\boldsymbol{x}_1$ is a subset of $\boldsymbol{x}$, including the design parameters related to the hydration and the microstructure of the CEAC; $\boldsymbol{z}$ is random Gaussian noise. The target $\boldsymbol{y}$ is the micro features of the CEAC. In this work, $\boldsymbol{y}$ is the synthetic XRD spectrum and the synthetic SEM images. In other words, the GAN part is designed to generate the XRD spectrum and the SEM images of the CEAC without an X-ray diffractometer and SEM, respectively.

The DNN part is considered as two functions $D(\boldsymbol{y},\boldsymbol{x}_2)$ and $A(\boldsymbol{f})$. The first one is $D(\boldsymbol{y},\boldsymbol{x}_2) \rightarrow \boldsymbol{f}$, where $\boldsymbol{x}_2$ is a subset of $\boldsymbol{x}$, including the design parameters of the CEAC related to its dry shrinkage behavior; $\boldsymbol{f}$ is a feature vector. Thus, the first function is used to extract the features related to the dry shrinkage behavior of the CEAC. The second function is $A(\boldsymbol{f}) \rightarrow \boldsymbol{d}$, where $\boldsymbol{d}$ is the dry shrinkage behaviors. Therefore, the framework finally characterize and predict the dry shrinkage behavior of the CEAC only using its design parameter set $\boldsymbol{x}$.

2.2. Generative adversarial network

GAN, first proposed by Radford et al. [40], has been widely used for automatic synthesis of realistic images from text [41,42]. In general, a GAN consists of a generator G and a discriminator D that

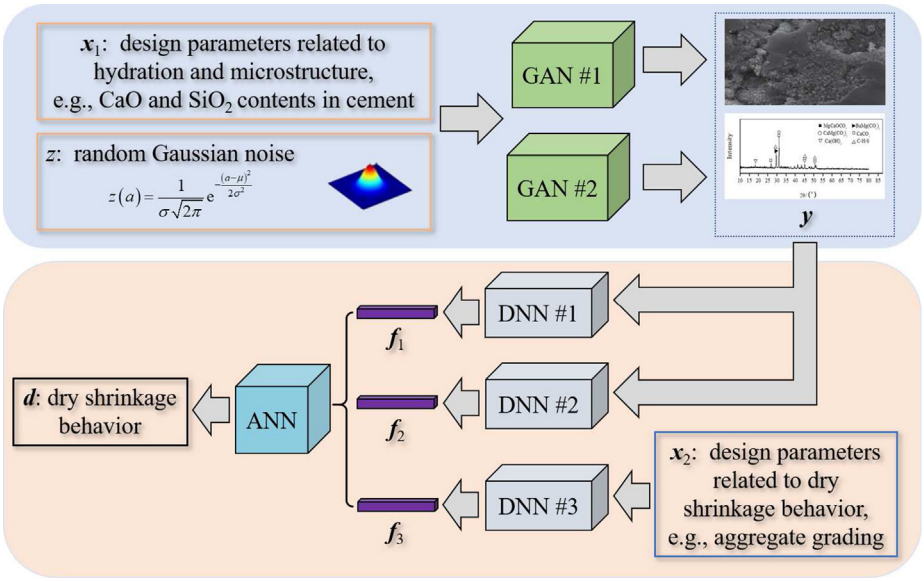

Fig. 1. Illustration of deep-learning framework.

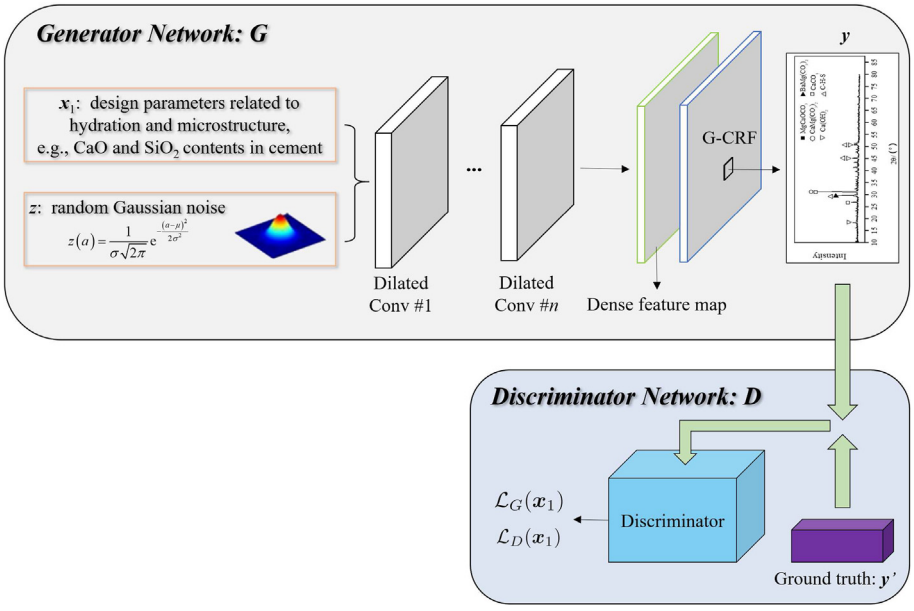

Fig. 2. Illustration of generative adversarial network.

play a minimax game, as shown in Fig. 2. The generator G tries to generate synthetic data based on a text description $\boldsymbol{x}$ and a random Gaussian noise $\boldsymbol{z}$. The synthetic data are used to fool the discriminator D. The discriminator D is trained to distinguish the synthetic data from the real ones. Therefore, the minimax game can be described as

$$\min_G \max_D V(D,G) = \mathbb{E}_{\boldsymbol{y}\prime\sim pt}[\log D(\boldsymbol{y}\prime)] + \mathbb{E}_{(\boldsymbol{x},\boldsymbol{z})\sim pf}[\log(1 - D(G(\boldsymbol{x},\boldsymbol{z})))], \quad (1)$$

where $\boldsymbol{y}\prime$ is the real data with the labeled probability distribution pt; $\boldsymbol{x}$ and $\boldsymbol{z}$ are a text description and a random Gaussian noise with the probability distribution pf, respectively.

In our study, two GANs, GAN #1 and GAN #2, are designed to generate XRD spectrums and SEM images based on the design parameters of a CEAC, respectively. The design parameters of a CEAC can be considered as a text description. The following notation is used in this study. A generator is denoted $G:\mathbb{R}^Z\times\mathbb{R}^{X_1}\to\mathbb{R}^D$ and $D:\mathbb{R}^D\times\mathbb{R}^Z\to\mathscr{L}$. Here, X_1 is the dimension of the design parameter subset $\boldsymbol{x}_1$ of a CEAC, which are related to its hydration and microstructure; Z is the dimension of a random Gaussian noise $\boldsymbol{z}$; D is the dimension of the synthetic XRD spectrum or images; $\mathscr{L}$ consists the losses of G and D.

In a generator G, random Gaussian noise $\boldsymbol{z}\in\mathbb{R}^Z\sim\mathcal{N}(0,1)$ is first generated and concatenated to $\boldsymbol{x}_1$. Then, the inference proceeds in the generator can be considered as a normal deconvolutional network: the set $(\boldsymbol{x}_1,\boldsymbol{z})$ is feeded through the layers in the deconvolutional network and the synthetic data $\boldsymbol{y}$ (XRD spectrums or SEM images) are generated via $G(\boldsymbol{x}_1,\boldsymbol{z})\to\boldsymbol{y}$. A normal deconvolutional network consists of several deconolutional layers, a condi-

tional random field, two support vector machines. For the complete mathematical introduction of a normal deconvolutional network, readers are invited to refer to our previous study [43].

In a discriminator D, three combination are first generated as $(\boldsymbol{x}_1,\boldsymbol{y})$, $(\boldsymbol{x}_1,\boldsymbol{y}')$, and $(\boldsymbol{wx}_1,\boldsymbol{y}')$, where $\boldsymbol{y}'$ is the real data (XRD spectrum or SEM image) from a CEAC whose partial design parameters are $\boldsymbol{x}_1$; and $\boldsymbol{wx}_1$ is wrong design parameters for the CEAC, which is generated randomly. Following this, the three combinations pass through several convolutional layers with stride-2 filters and spatial batch normalization [44]. These convolutional layers are used to reduce the dimension of the three combination. Then, the final loss $\mathscr{L}_G$ and $\mathscr{L}_D$ for $\boldsymbol{x}_1$ is computed as

$$\mathscr{L}_G(\boldsymbol{x}_1) = -\log(D(\boldsymbol{x}_1,\boldsymbol{y})), \tag{2}$$

and

$$\mathscr{L}_D(\boldsymbol{x}_1) = -\log(D(\boldsymbol{x}_1,\boldsymbol{y}\prime)) - \frac{\log(1-D(\boldsymbol{x}_1,\boldsymbol{y})) + \log(1-D(\boldsymbol{wx}_1,\boldsymbol{y}\prime))}{2}. \tag{3}$$

With the final loss $\mathscr{L}_G$ and $\mathscr{L}_D$, the parameters in G and D can be updated via minibatch stochastic gradient descent. The database for training GAN #1 and #2 in this work are introduced in Section 3.1.

2.3. Deep neural network

DNN, as the most successful case of deep learning [45,46], is mostly used to map complex data (e.g., images [47,48] and signals [49,50]) to target values. As shown in Fig. 1, the DNN part in the proposed framework is made up of three parts: three DNNs with only convolutional and pooling layers, a feature concatenator, and an artificial neural network (ANN). The proposed DNN part can be summarized as three steps as follows. Step 1 The synthetic XRD spectrum, the synthetic SEM images, and the design parameters related to the dry shrinkage behaviors $\boldsymbol{x}_2$ are imported into DNN #1, DNN #2, and DNN #3, respectively. In each DNN, a convolution layer is followed by a pooling layer. A pairwise combination of a convolution layer and a pooling layer is a block. The convolution operation processes in a block l can be described as

$$z_{u,v}^{l,c} = \sum_{i=-\infty}^{\infty}\sum_{j=-\infty}^{\infty} x_{i+u,j+v}^{l-1}\cdot k_{j,i}^{l,c}\cdot\chi(i,j) + B^{l,c}, \tag{4a}$$

$$\chi(i,j) = \begin{cases} 1, & 0\leqslant i,j\leqslant \min(a,b) \\ 0, & other, \end{cases} \tag{4b}$$

$$a_{u,v}^{l,c} = \begin{cases} z_{u,v}^{l,c}, & z_{u,v}^{l,c}\geqslant 0 \\ 0, & z_{u,v}^{l,c}\leqslant 0, \end{cases} \tag{4c}$$

and the pooling operation processes in the block l is defined by the following equations:

$$y_{i,j}^{l,c} = \sum_{u=ir}^{(i+1)r-1}\sum_{v=jr}^{(j+1)r-1}\gamma_{u,v}^{l,c}\cdot a_{u,v}^{l,c} + b^{l,c}, \tag{5a}$$

$$p_{i,j}^{l,c} = Sigmoid(y_{i,j}^{l,c}). \tag{5b}$$

In Eq. 4a, $x_{i+u,j+v}^{l-1}$ is the element of the input data $\boldsymbol{X}^{l-1}$ in the $(i+u)$-th row and $(j+v)$-th column; $k_{j,i}^{l,c}$ is the weight of the convolution kernel matrix $\boldsymbol{K}^{l,c}$ with the size $a\times b$ in the j-th row and i-th column, for $c=1,\ldots,C$; C is the kernel number in the block l; $B^{l,c}$ is the bias of the convolution kernel matrix $\boldsymbol{K}^{l,c}$. In Eq. 5a, $b^{l,c}$ is the bias in pooling layer; $\gamma_{u,v}^{l,c}$ for two widely-used pooling is expressed as.[Average pooling:] $\gamma_{u,v}^{l,c} = \frac{1}{r\times r}$ [Max pooling:] $\gamma_{u,v}^{l,c} = \begin{cases} 1, & \max\{a_{u,v}^{l,c},\cdots,a_{u+r-1,v+r-1}^{l,c}\} \\ 0, & others \end{cases}$. Step 2 The outputs of the three DNNs ($\boldsymbol{f}_1$,$\boldsymbol{f}_2$, and $\boldsymbol{f}_3$) are concatenated as a vector $\boldsymbol{f}=\{\boldsymbol{f}_1,\boldsymbol{f}_2,\boldsymbol{f}_3\}$. Step 3 The concatenated vector $\boldsymbol{f}$ is imported into an ANN and mapped to the dry shrinkage behaviors as

$$N_\eta^\delta = tanh\left(\sum_{k=1}^{\epsilon} f_k^{\delta-1}\cdot\omega_{k,\eta}^\delta + \kappa_k^\delta\right), \quad \eta=1,\ldots,H, \tag{6}$$

where, N_η^δ is the output of the neuron η in the fully connected layer $\delta, \delta=1,\ldots,\Delta$; H is the neuron number in the layer; $f_k^{\delta-1}$ is the element k in the input vector $f^{\delta-1}$ of the layer δ; $\omega_{k,\eta}^\delta$ is the connect weight between the neuron η in the layer δ and the neuron η in the layer $\delta-1$; κ_k^δ is the bias of the neuron η.

The final loss of the ANN $\mathscr{L}_A$ for $\boldsymbol{f}$ is computed as

$$\mathscr{L}_A(\boldsymbol{f}) = \left\|\boldsymbol{N}^\Delta - \boldsymbol{d}\right\|_2^2, \tag{7}$$

where $\boldsymbol{N}^\Delta$ is the output vector of the final layer in the ANN; $\boldsymbol{d}$ is the real dry shrinkage behaviors. With the final loss $\mathscr{L}_A$, the parameters in the three DNNs and the ANN can be updated via minibatch stochastic gradient descent. The database for training the DNN part in this work are introduced in Section 3.1.

3. Experimental details

In this chapter, the information of training the deep-learning framework is introduced in Section 3.1. The details about the testing experiments for the well-trained framework are described in Section 3.2.

3.1. Training information

In this study, 835 groups of CEACs were collected, a part of which has been reported in the previous studies, such as [5,9,18]. With the randomly generated Gaussian noise $\boldsymbol{z}$, the group number was extended to 2505. During training, 25% of the 2505 groups were selected as a validation set, which is used to verify whether a GAN is well trained or not in Section 4.1. In the validation set, the ratio of the three combination inputs ($(\boldsymbol{x}_1,\boldsymbol{y})$, $(\boldsymbol{x}_1,\boldsymbol{y}\prime)$, and $(\boldsymbol{wx}_1,\boldsymbol{y}\prime)$) was about 1:1:1. The detailed information of GANs, DNNs, an ANN used in the experiment are shown in Table 1–3.

As introduced in Section 2, the information of each CEAC was assigned to $\boldsymbol{x}_1,\boldsymbol{x}_2,\boldsymbol{y}\prime$, and $\boldsymbol{d}$. Here, $\boldsymbol{x}_1$ was a set of the design parameters of a CEAC, which influenced on its hydration and microstructure. The elements in $\boldsymbol{x}_1$ represented the parameters in the following order.

- Mix ratio: the mass fractions of cement, asphalt, water, and aggregates;
- Chemical compositions of cement: the mass fractions of SiO_2, CaO, Al_2O_3, Fe_2O_3, MgO, SO_3, Na_2O_{eq}, f-CaO, C_3S, C_2S, C_3A, and C_4AF;
- Properties of cement: fineness (residue on 80 μm sieve) and setting time;
- Properties of asphalt: residue masses by distillation and on 1.18 mm sieve;
- Properties of aggregates: the mass fractions of CaO and SiO_2;
- Curing condition: only curing time is considered in this study because these CEACs are always cured in a standard environmental condition (20 ± 2 °C and 90% relative humidity).

For $\boldsymbol{x}_2$, it included the design parameters related to the dry shrinkage behavior of a CEAC as follow.

Table 1
Detailed information of GAN #1.

Part	Layer number	Layer type	Input	Kernel	Stride	Padding	Output
Generator	#1	Input	$\boldsymbol{x}$ of the size 1 × 1 × 23 with/without $\boldsymbol{z}$	–	–	–	1 × 1 × 23
	#2	Deconvolution	1 × 1 × 23	1 × 5 × DeConv. 64 *ReLU*	1 × 3	3	1 × 10 × 64
	#3	Deconvolution	1 × 10 × 64	1 × 5 × DeConv. 32 *ReLU*	1 × 3	3	1 × 37 × 32
	#4	Deconvolution	1 × 37 × 32	1 × 5 × DeConv. 16 *ReLU*	1 × 3	2	1 × 118 × 16
	#5	Deconvolution	1 × 118 × 16	1 × 3 × DeConv. 8 *ReLU*	1 × 2	1	1 × 236 × 8
	#6	Deconvolution	1 × 236 × 8	1 × 3 × DeConv. 4 *ReLU*	1 × 2	1	1 × 472 × 4
	#7	Deconvolution	1 × 472 × 4	1 × 3 × DeConv. 2 *ReLU*	1 × 1	1	1 × 473 × 2
	#8	Deconvolution	1 × 473 × 2	1 × 1 × DeConv. 1 *ReLU*	1 × 1	1	1 × 473 × 1
Discriminator	#9	Convolution	1 × 473 × 1	1 × 3 × Conv. Maxout 32 *ReLU*	1 × 2	1	1 × 237 × 32
	#10	Pooling	1 × 237 × 32	1 × 2 mean pooling	1 × 2	1	1 × 119 × 32
	#11	Convolution	1 × 119 × 32	1 × 3 × Conv. Maxout 64 *ReLU*	1 × 2	1	1 × 59 × 64
	#12	Pooling	1 × 59 × 64	1 × 2 mean pooling	1 × 2	1	1 × 30 × 64
	#13	Convolution	1 × 30 × 64	1 × 3 × Conv. Maxout 128 *ReLU*	1 × 2	1	1 × 15 × 128
	#14	Pooling	1 × 15 × 128	1 × 2 mean pooling	1 × 2	1	1 × 8 × 128
	#15	Convolution	1 × 8 × 128	1 × 3 × Conv. Maxout 256 *ReLU*	1 × 2	1	1 × 3 × 256
	#16	Convolution	1 × 3 × 256	1 × 3 × Conv. Maxout 256 *ReLU*	1 × 1	1	1 × 1 × 256
	#17	Convolution	1 × 1 × 256	1 × 1 × Conv. Maxout 256 *ReLU*	1 × 1	1	1 × 1 × 256
	#18	Fully connection	1 × 1 × 256	256 × 1024*Sigmod*	–	–	1 × 1 × 1024
	#19	Fully connection	1 × 1 × 1024	1024 × 2 *Sigmod*	–	–	1 × 1 × 2
	#20	Softmax	1 × 1 × 2	–	–	–	–

Table 2
Detailed information of GAN #2.

Part	Layer number	Layer type	Input	Kernel	Stride	Padding	Output
Generator	#1	Input	$\boldsymbol{x}$ of the size 1 × 1 × 23 with/without $\boldsymbol{z}$	–	–	–	1 × 1 × 23
	#2	Deconvolution	1 × 1 × 23	3 × 3 × DeConv. 64 *ReLU*	2 × 2	1	46 × 46 × 64
	#3	Deconvolution	1 × 1 × 23	5 × 5 × DeConv. 64 *ReLU*	3 × 3	3	10 × 10 × 64
	#4	Deconvolution	10 × 10 × 64	5 × 5 × DeConv. 32 *ReLU*	3 × 3	3	37 × 37 × 32
	#5	Deconvolution	37 × 37 × 32	5 × 5 × DeConv. 16 *ReLU*	3 × 3	2	118 × 118 × 16
	#6	Deconvolution	118 × 118 × 16	3 × 3 × DeConv. 8 *ReLU*	2 × 2	1	236 × 236 × 8
	#7	Deconvolution	236 × 236 × 8	3 × 3 × DeConv. 4 *ReLU*	2 × 2	1	472 × 472 × 4
	#8	Deconvolution	472 × 472 × 4	3 × 3 × DeConv. 2 *ReLU*	1 × 1	1	473 × 473 × 2
Discriminator	#9	Deconvolution	473 × 473 × 2	1 × 1 × DeConv. 1 *ReLU*	1 × 1	1	473 × 473 × 1
	#10	Convolution	473 × 473 × 1	3 × 3 × Conv. Maxout 32 *ReLU*	2 × 2	1	237 × 237 × 32
	#11	Pooling	237 × 237 × 32	2 × 2 max pooling	2 × 2	1	119 × 119 × 32
	#12	Convolution	119 × 119 × 32	3 × 3 × Conv. Maxout 64 *ReLU*	2 × 2	1	59 × 59 × 64
	#13	Pooling	59 × 59 × 64	2 × 2 max pooling	2 × 2	1	30 × 30 × 64
	#14	Convolution	30 × 30 × 64	3 × 3 × Conv. Maxout 128 *ReLU*	2 × 2	1	15 × 15 × 128
	#15	Pooling	15 × 15 × 128	2 × 2 max pooling	2 × 2	1	8 × 8 × 128
	#16	Convolution	8 × 8 × 128	3 × 3 × Conv. Maxout 256 *ReLU*	2 × 2	1	3 × 3 × 256
	#17	Convolution	3 × 3 × 256	3 × 3 × Conv. Maxout 256 *ReLU*	1 × 1	1	1 × 1 × 256
	#18	Convolution	1 × 1 × 256	1 × 1 × Conv. Maxout 256 *ReLU*	1 × 1	1	1 × 1 × 256
	#19	Fully connection	1 × 1 × 256	256 × 1024*Sigmod*	–.	.–	1 × 1 × 1024
	#20	Fully connection	1 × 1 × 1024	1024 × 2 *Sigmod*	.–	.–	1 × 1 × 2
	#21	Softmax	1 × 1 × 2	–.	.–	.–	.–

- Properties of cement: 3 and 28 day compression strength, mass contents of SiO_2 and CaO, and setting time;
- Properties of asphalt: penetration degree (25 °C, 100 g, and 5 s), softening point, and ductility (25 °C);
- Properties of aggregates: Aggregate grading, apparent specific gravity, crushed value, weared value, and adhesion grade with asphalt.

The set $\boldsymbol{y}_{\prime}$ consisted of two part: the real SEM images and the real XRD spectrum of each CEAC. For $\boldsymbol{d}$, it was the dry shrinkage rate of the CEAC in the study. Both of $\boldsymbol{y}_{\prime}$ and $\boldsymbol{d}$ were used to compare with the synthetic data from the two GANs.

A random gradient descent algorithm with mini-batches of size 10 was performed on all of the architectures in Table 1–3 during training. Logarithmically decreasing learning rates were adopted with a base learning rate of 0.01. The momentum and weight decay were 0.9 and 0.005, respectively. The proposed framework was trained via TensorFlow. The above procedures were performed on a computer that was equipped with an Intel (R) Core (TM) i7-8750H CPU, 32.00 GB RAM, and an NVIDIA GeForce GTX 1080 8 GB GPU.

3.2. Testing experiments

In this work, 36 groups of CEACs were designed to test the effectiveness of the well-trained deep-learning framework, as shown in Table 4. Fig. 3 and Table 5–8 present the parameters of the 36 groups. The real XDR spectrums, SEM images, and dry shrinkage rates of the 36 groups were measured to compare with the synthetic data and the predicted dry shrinkage ratios.

In each group, twelve samples were replicated. The samples were uniformly split into three sub-groups with different curing days (3-day, 7-day, 14-day, and 28-day). One of the samples in a sub-group was randomly selected to perform the XDR-spectrum test and SEM observation. All three samples in a sub-group were used to measure their dry shrinkage ratios after curing, and the dry shrinkage ratio of the sub-group was the averaged one. The

Table 3
Detailed information of DNNs and ANN.

Parts	Layer number	DNN #1	DNN #2	DNN #3
DNNs	#1	1 × 3 × Conv. Maxout 32 *ReLU* with 2 strides	3 × 3 × Conv. Maxout 32 *ReLU* with 2 strides	21 × 64 Fully connection *Sigmod*
	#2	1 × 2 mean pooling with 2 strides	2 × 2 max pooling with 2 strides	64 × 256 Fully connection *Sigmod*
	#3	1 × 3 × Conv. Maxout 64 *ReLU* with 2 strides	3 × 3 × Conv. Maxout 64 *ReLU* with 2 strides	256 × 1024 Fully connection *Sigmod*
	#4	1 × 2 mean pooling with 2 strides	2 × 2 max pooling with 2 strides	1024 × 256 Fully connection *Sigmod*
	#5	1 × 3 × Conv. Maxout 128 *ReLU* with 2 strides	3 × 3 × Conv. Maxout 128 *ReLU* with 2 strides	256 × 32 Fully connection *Sigmod*
	#6	1 × 2 mean pooling with 2 strides	2 × 2 max pooling with 2 strides	–
	#7	1 × 3 × Conv. Maxout 256 *ReLU* with 2 strides	3 × 3 × Conv. Maxout 256 *ReLU* with 2 strides	–
	#8	1 × 3 × Conv. Maxout 256 *ReLU* with 1 strides	3 × 3 × Conv. Maxout 256 *ReLU* with 1 strides	–
	#9	1 × 1 × Conv. Maxout 256 *ReLU* with 1 strides	1 × 1 × Conv. Maxout 256 *ReLU* with 1 strides	–
	#10	256 × 1024*Sigmod*	256 × 1024*Sigmod*	–
	#11	1024 × 64*Sigmod*	1024 × 64*Sigmod*	–
Feature concatenator	#12	64 + 64 + 32 = 160		
ANN	#13	160 × 256*Sigmod*		
	#14	256 × 512*Sigmod*		
	#15	512 × 32 *Sigmo*		
	#16	32 × 1 *Regression*		

Table 4
Testing experiments.

No.	Mix ratio			Chemical compostions and properties of cement (Table 5 and Table 6)	Aggregate grading (Fig. 3 and Table 8)	Curing time/day
	Cement	Asphalt	Water			
I1	1	6	2	Cement 1	Grading 1	3
I2	1	6	2	Cement 2	Grading 2	7
I3	1	6	2	Cement 1	Grading 2	14
I4	1	6	2	Cement 2	Grading 1	28
II1	1	7	1	Cement 1	Grading 1	3
II2	1	7	1	Cement 2	Grading 2	7
II3	1	7	1	Cement 1	Grading 2	14
II4	1	7	1	Cement 2	Grading 1	28
III1	1	8	0	Cement 1	Grading 1	3
III2	1	8	0	Cement 2	Grading 2	7
III3	1	8	0	Cement 1	Grading 2	14
III4	1	8	0	Cement 2	Grading 1	28
IV1	2	6	3	Cement 1	Grading 1	3
IV2	2	6	3	Cement 2	Grading 2	7
IV3	2	6	3	Cement 1	Grading 2	14
IV4	2	6	3	Cement 2	Grading 1	28
V1	2	7	1	Cement 1	Grading 1	3
V2	2	7	1	Cement 2	Grading 2	7
V3	2	7	1	Cement 1	Grading 2	14
V4	2	7	1	Cement 2	Grading 1	28
VI1	2	8	0	Cement 1	Grading 1	3
VI2	2	8	0	Cement 2	Grading 2	7
VI3	2	8	0	Cement 1	Grading 2	14
VI4	2	8	0	Cement 2	Grading 1	28
VII1	3	6	4	Cement 1	Grading 1	3
VII2	3	6	4	Cement 2	Grading 2	7
VII3	3	6	4	Cement 1	Grading 2	14
VII4	3	6	4	Cement 2	Grading 1	28
VIII1	3	7	2	Cement 1	Grading 1	3
VIII2	3	7	2	Cement 2	Grading 2	7
VIII3	3	7	2	Cement 1	Grading 2	14
VIII4	3	7	2	Cement 2	Grading 1	28
IX1	3	8	2	Cement 1	Grading 1	3
IX2	3	8	2	Cement 2	Grading 2	7
IX3	3	8	2	Cement 1	Grading 2	14
IX4	3	8	2	Cement 2	Grading 1	28

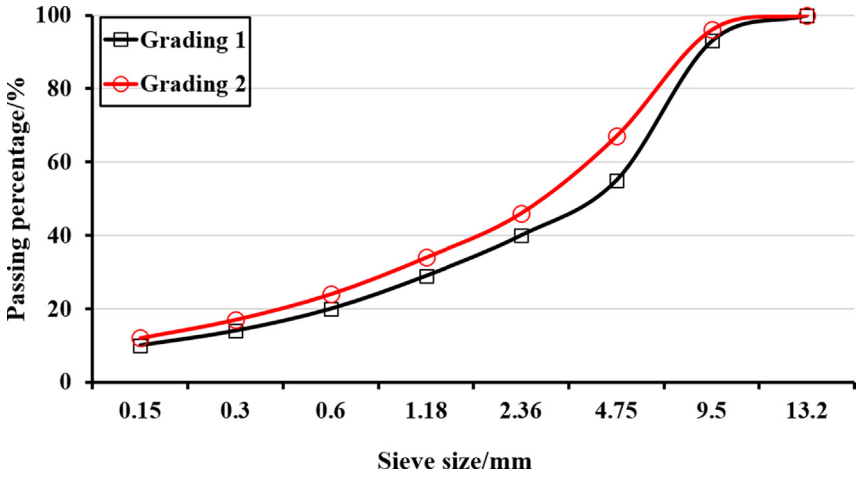

Fig. 3. Aggregate grading.

Table 5
Chemical composition of the cements/%.

	SiO_2	CaO	Al_2O_3	Fe_2O_3	MgO	SO_3	Na_2Oeq	*f*-CaO	C_3S	C_2S	C_3A	C_4AF
Cement 1	21.88	65.89	4.61	2.52	1.76	1.77	0.59	0.98	60.22	17.33	7.63	8.52
Cement 2	25.21	70.62	1.24	0.72	1.15	0.1	0.18	0.78	62.32	16.24	6.82	7.3

dry shrinkage ratio of a sample was measured after curing with a temperature of $(20 \pm 2)^{\circ}C$ and a humidity of $(60 \pm 5)\%$.

4. Results and discussion

4.1. Characterization of hydration and microstructure

4.1.1. Performance of the XDR-spectrum and SEM-image synthesis

Before the use of the deep-learning framework, we first verified the effectiveness of the XDR-spectrum and SEM-image synthesis. Fig. 4 presents the losses of the validation data set during the GAN training processes. The validation data set was randomly selected from the training database introduced in Section 3.1, whose size was 25% of the training database. At the beginning of the training, $\mathscr{L}_D$ was less than 0.001. It demonstrated that the three combination inputs $((\boldsymbol{x}_1, \boldsymbol{y}), (\boldsymbol{x}_1, \boldsymbol{y}')$, and $(\boldsymbol{wx}_1, \boldsymbol{y}'))$ were not able to fool the discriminator *D*. Thus, *D* easily distinguished the synthetic SEM images and the synthetic XDR spectrums from the real data. This was because a well-trained *D* was used to guarantee the quality of the training [51], and the generated samples from *G* at the start were extremely poor, and they were rejected by *D* with high confidence. With the update of the parameters in $G, \mathscr{L}_D$ increased. It meant that the outputs of *D* $(D(\boldsymbol{x}_1, \boldsymbol{y}), D(\boldsymbol{x}_1, \boldsymbol{y}')$, and $D(\boldsymbol{wx}_1, \boldsymbol{y}'))$ were close to $(0, 1, 0)$. It indicated that *D* had no confidence to distinguish $(\boldsymbol{wx}_1, \boldsymbol{y}')$ and $(\boldsymbol{x}_1, \boldsymbol{y})$ from $(\boldsymbol{x}_1, \boldsymbol{y}')$ after training. In addition, the final loss of *G* based on Eq. 2 ($\mathscr{L}_G \approx 0$) also demonstrated this phenomenon.

The two losses, $\mathscr{L}_D$ and $\mathscr{L}_G$, only reflected the successful fooling of *D* via the generated data from *G*. We should further measure the gap between $\boldsymbol{y}$ and $\boldsymbol{y}\prime$. A small gap can guarantee that the synthetic

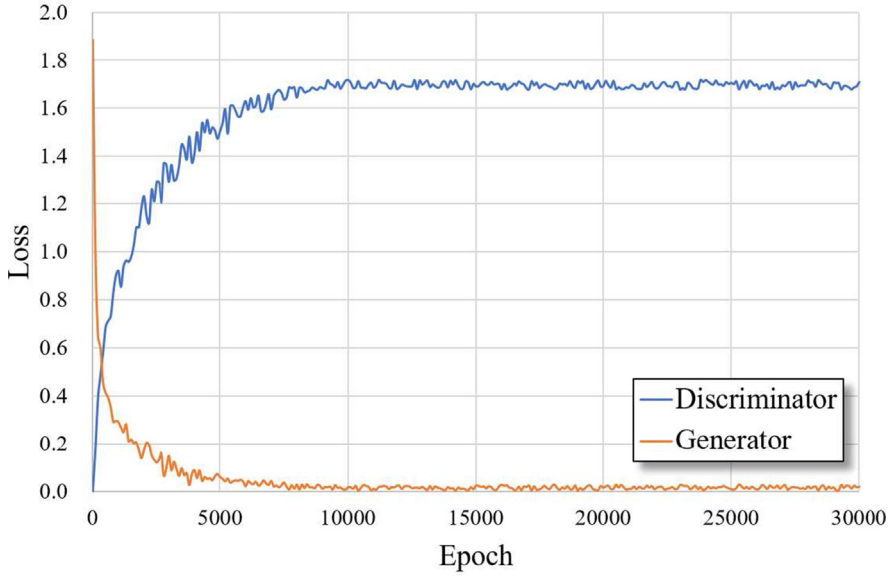

Fig. 4. Losses of the validation data set during the GAN training.

data characterize the hydration and microstructure of a CEAC as well as the real data from a X-ray diffractometer and a SEM. First, the average Euclidean distance $d(\boldsymbol{y},\boldsymbol{y}')$ between the synthetic and real XDR spectrums of CEACs was measure as

$$d(\boldsymbol{y},\boldsymbol{y}') = \frac{1}{n}\sum_{i=1}^{n}\sqrt{\frac{1}{m}\sum_{2\theta=15^\circ}^{55^\circ}(\boldsymbol{y}'_i(2\theta)-\boldsymbol{y}_i(2\theta))^2}, \tag{8}$$

where $\boldsymbol{y}'(2\theta)$ and $\boldsymbol{y}(2\theta)$ are the intensity values in the synthetic and real XDR spectrums, respectively; 2θ is the angle between incident and diffracted X-rays; n is the sample number in the validation data set; and m is the total number of sampling angles. The well-trained GAN finally achieved an average Euclidean distance less than 0.001 when the intensity values in the spectrums were normalized by the maximum one. It indicated that the synthetic and real XDR spectrums in the validation data set were highly close.

Fig. 5 presents the receiver operating characteristic curves (ROCs) of the well-trained GAN for generating SEM images. A ROC curve measures how much a model is capable of distinguishing between classes by plotting the true positive rate (TPR) against the false positive rate (FPR) at various threshold settings. In machine learning, TPR, also known as *recall*, is the ratio of true positive over the sum of the true positive and the false negative. FPR is also called *probability of false alarm* and is defined as the ratio of false-positive over the sum of true negative and false positive. The ROC curve is thus the recall as a function of fall-out. In Fig. 5, the hydrates are considered as positives, while the rests of the components are regarded as background, which were negatives in the study. Thus, a ROC far from the text line in Fig. 5 indicated the good performance of a GAN. More information about ROC analysis can be found in [52]. As expected, the ROCs of hydrates and background were far from the text line. It demonstrated that the GAN part had the capacity to generate SEM images, which could characterize the hydration products and background in the microstructure of CEACs. In addition, the capacity of generating background was better than the capacity of generating hydration products, demonstrating the generation of the background needed less information from the design parameter set $\boldsymbol{x}_1$ than the generation of the hydrates. Thus, it is a potential way to include more design parameters in $\boldsymbol{x}_1$ to improve the characterization capacity for hydrates in the synthetic SEM images.

In summary, the results mentioned above demonstrated that the GAN part was capable of mapping the design parameters of a CEAC to its XRD spectrum and SEM images. With the assistance of the GAN part, it was possible to predict the hydration and microstructure of a CEAC only using its design parameters.

4.1.2. Characterization of hydration and microstructure

Fig. 6 presents the synthetic XDR spectrums of the 36 testing groups. These synthetic data could characterize the hydration processes of CEACs. For example, the three main diffraction peaks at about $18^\circ, 34^\circ, 47^\circ$ were related to the diffraction of cement hydration productions and calcium hydroxide (portlandite). High diffraction peaks at the three angles indicated a good crystallization of cement hydration productions and portlandite. The contents of portlandite increased with the increase of the cement content or the decrease of the asphalt content. The synthetic XDR spectrums of the groups with the different types of cement had some differences. For example, the synthetic XDR spectrums of the CEACs with Cement 2 had the diffraction peaks at about 45° with smaller values of intensity than those of the CEACs with Cement 1 had. It showed that the use of different types of cement had the effects on the hydration processes and the hydrates because of their different chemical compositions. Besides, there were only inapparent changes of the diffraction peaks at about 32°. A peak at about 32° is related to the diffraction of $CaCO_3$. It indicated that the peaks were not caused by the hydration but by the chemical compositions of the aggregates. In addition, the effects of the ratio between cement and water could also be found in these synthetic data. Hydration characterization could be conducted with the synthetic XDR spectrums, which were close to the real spectrums. This section just provides some examples of the characterization.

Fig. 7 presents examples of synthetic SEM images. These images are generated by the well-trained GAN part using the design parameters of Group II1 and different random Gaussian noises. In

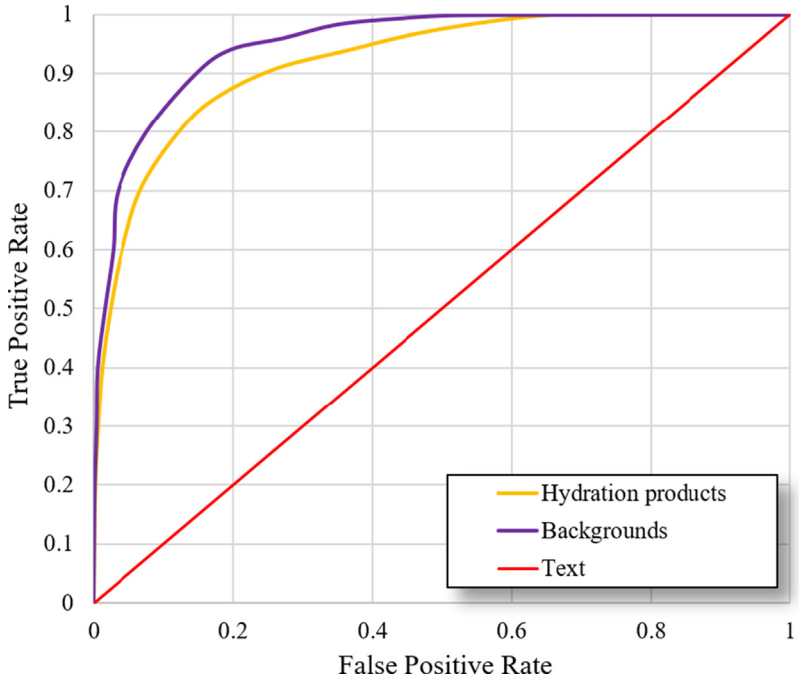

Fig. 5. ROC curves of GAN for generating SEM images with *True Positive Rate* $= \frac{True\ Positive}{True\ Positive+False\ Negative}$ and *False Positive Rate* $= \frac{False\ Positive}{False\ Positive+True\ Negative}$.

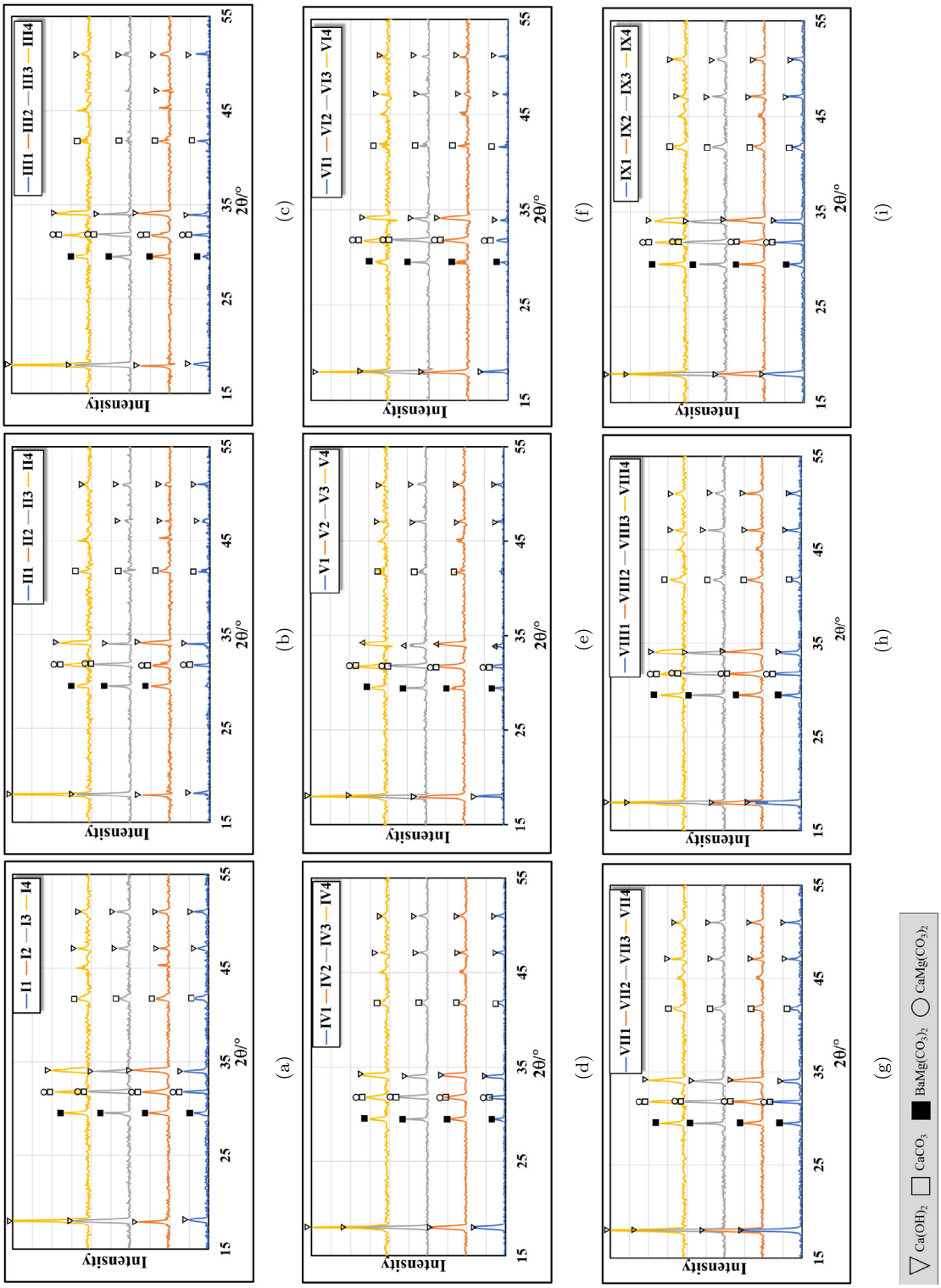

Fig. 6. Synthetic XDR spectrums.

Fig. 7, cement hydrates, asphalt, pore, others can be distinguished clearly. Thus, the synthetic images had the capacity of characterizing the microstructure of CEACs qualitatively. Considering that the synthetic images are very close to the real SEM images, a deep-learning method has the potential to characterize the microstructure information of the CEACs. In the method, different components in SEM images are first extracted by a fully convolutional network. The extracted components are then used to characterize the microstructure. For the complete information about the method, readers are invited to read our previous studies [36,38].

4.2. Characterization of dry shrinkage behavior

Fig. 8 presents the predicted and measured dry shrinkage ratios of the 36 groups. The average and maximum errors between the predicted and measured results were 2.70% and 4.29%. It demon-

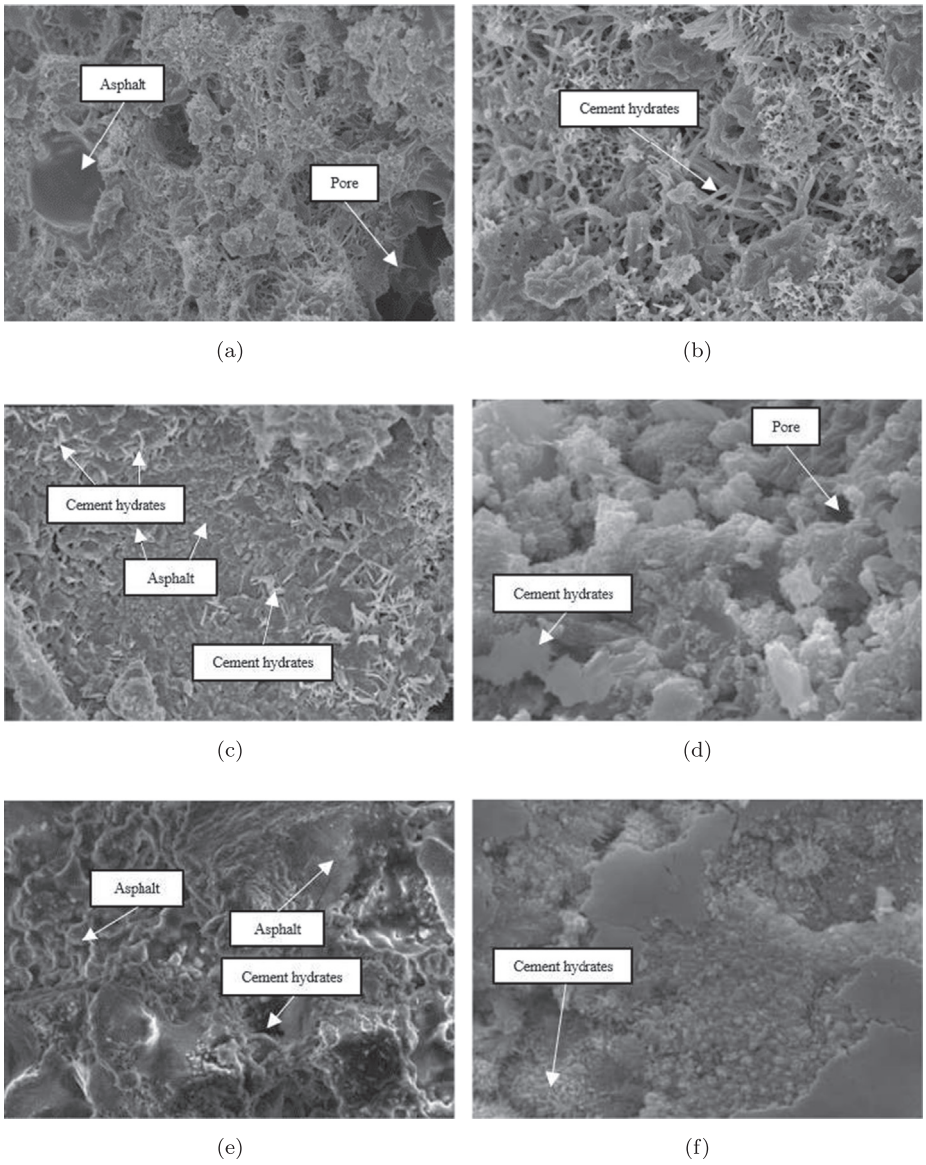

Fig. 7. Synthetic SEM images.

strated the high and stable precision of the well-trained DNN part for predicting the dry shrinkage ratios. Compared with the traditional studies using ANN, the proposed DNN part considered the hydration and the microstructure of the CEACs via the synthetic XRD spectrums and SEM images, which had the potential to improve the accuracy. In addition, the DNN part thoroughly considered the influence of many other factors, such as aggregate grading and curing condition.

A comparison study was also performed to demonstrate the advantages of the proposed framework in the characterization of dry shrinkage behavior. In the comparison study, we selected two other methods to predicted the dry shrinkage ratios of the 36 groups. The first was a rule-based method [5,9,18], which used some functions w.r.t the design parameters of CEACs to predict the dry shrinkage ratios. Another was ANN-based methods, which was also a data-driven method as the proposed framework but only used an ANN to perform the characterization. The used ANN had the same architecture as the one in the proposed framework, as shown in Table 3. The used ANN was also trained by the training set introduced in Section 3.1. The proposed framework achieved the minimum errors in the 36 testing groups, followed by the ANN-based and rule-based methods (Fig. 8). This demonstrated the proposed framework was advantageous in the characterization of dry shrinkage behavior of CEACs. Tables 6,7,8.

With the predicted dry shrinkage ratios, it could be found that the dry shrinkage ratio decreased with the increase of the cement and water contents. For example, the 7-day and 28-day dry shrinkage ratios of these CEACs decreased when the cement content increased from 1% to 3%. Besides, emulsified asphalt had negative effects on the dry shrinkage behavior of the CEACs. For example, the 7-day and 28-day dry shrinkage ratios increased when the emulsified asphalt content increased from 6% to 7%. This was because of the space-charge effects between cement and emulsified asphalt. To be precise, cement particles adsorbed the water phase of the emulsified asphalt as the reaction water, which promoted the cement hydration and accelerated the demulsification of emulsified asphalt. The cement hydrates filled the gaps of the CEACs to reduce the dry shrinkage. In addition, the effects of other factors (e.g., aggregate grading and curing condition) were also characterized by the predicted dry shrinkage ratios.

A t-distributed stochastic neighbor embedding (t-SNE) [53] was used to characterize the dry shrinkage behavior of the CEACs. A

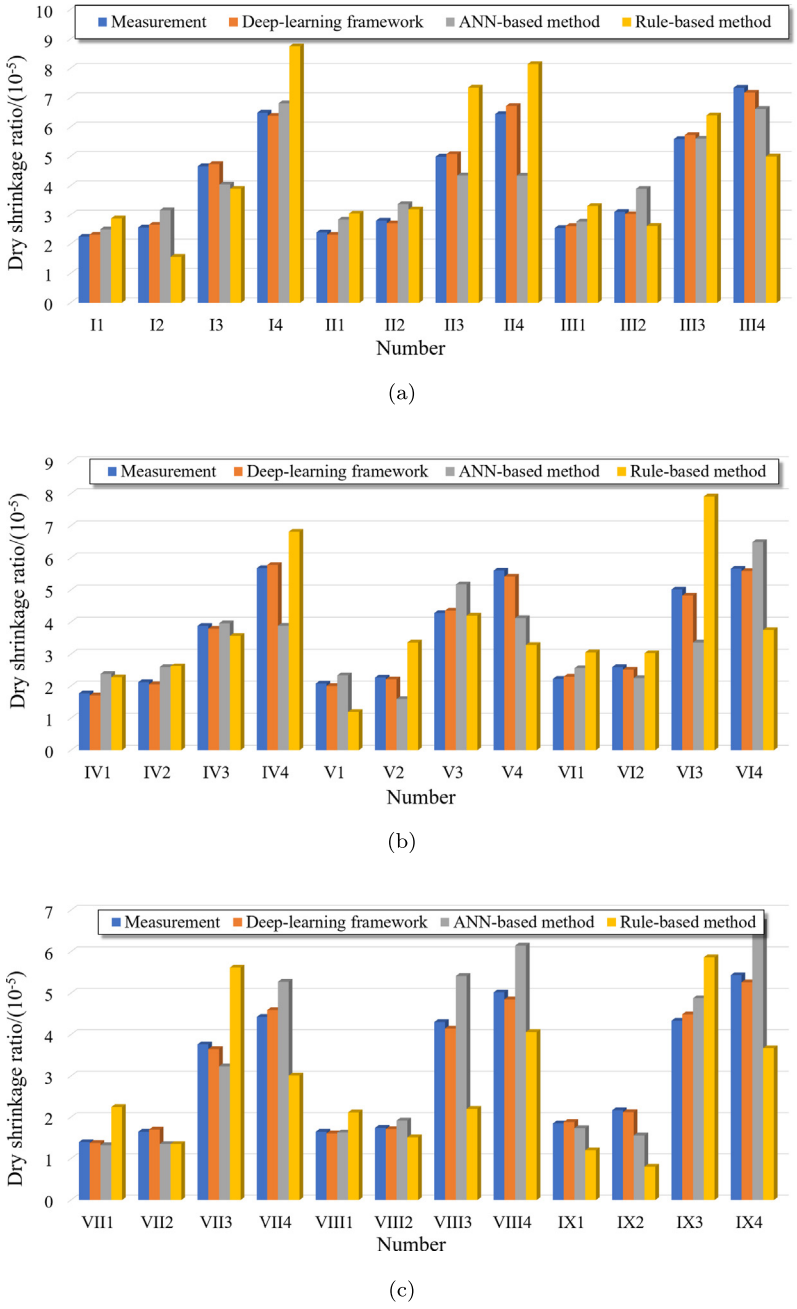

Fig. 8. Prediction and measurement results of dry shrinkage ratios: (a) 6% emulsified asphalt content, (b) 7% emulsified asphalt content, and (c) 8% emulsified asphalt content.

Table 6
Properties of the ordinary Portland cements.

	Fineness (residue on 80 μm sieve)	Setting time/min		Compression strength/ MPa	
		Initial	Final	3 day	28 day
Cement 1	2.781	149	221	28.7	49.5
Cement 2	2.977	132	214	31.4	54.9

Table 7
Test results of the emulsified asphalt.

Residue by distillation/%	1.18 *mm* sieve test/%	Penetration (25 °C, 100 g, and 5 s)/0.1 *mm*	Softening point/°C	Ductility (25 °C)/cm
62	0.03	84	46	45

Table 8
Aggregate properties

Apparent specific gravity/(g · cm^{-3})	Crushed value/%	Weared value			
%	Adhesion grade with asphalt	CaO content/%	SiO_2 content/%		
2.804	8	14.9	4	35.05	11.59

t-SNE algorithm models each high-dimensional representation of objects by a two- or three-dimensional point in such a way that similar objects are modeled by nearby points and dissimilar objects are modeled by distant points with high probability. First, t-SNE constructs a probability distribution over pairs of high-dimensional features of samples in such a way that similar objects are assigned a higher probability while dissimilar points are assigned a lower probability. Second, t-SNE defines a similar probability distribution over the points in the low-dimensional map, and it minimizes the Kullback–Leibler divergence between the two distributions with respect to the locations of the points in the map. Thus, the similarity of two samples can be characterized by their Euclidean distance in the t-SNE mapping. A feature vector $\boldsymbol{f}$ introduced in *Step* 1 of Section 2.3 could be considered as the representation of a CEAC related to its dry shrinkage behavior. However, the dimension of $\boldsymbol{f}$ is 512, which led it not visible. Thus, all feature vectors of the training samples and the 36 testing groups were mapped to a two-dimensional feature space via t-SNE. Each point in Fig. 9 represents a feature vector corresponding to a CEAC. Fig. 9a presents the distribution of the 2505 training samples in the t-SNE two-dimensional feature space. The feature vectors spanned the feature space and were evenly distributed in the space. It indicated that the feature vectors could be used to differentiate CEACs effectively. Feature vectors gathered round in the space if the corresponding dry shrinkage ratios were close. From the distribution of the 36 testing feature vectors, as shown in Fig. 9b, we concluded that the curing time had the most significant effects on the dry shrinkage ratios, followed by the aggregate grading and the contents of cement and emulsified asphalt. The curing time mainly influenced the hydration processes, while the aggregate grading directly influenced the porosity of the composites. The influence of other factors was also reflected in Fig. 9b. For example, the effects of aggregate grading were slightly higher than those of the asphalt and cement contents since the groups with the same grading were clustered more significantly that those with the same contents of asphalt and cement. Thus, the feature vectors were capable of characterizing the dry shrinkage behaviors of these CEACs. In summary, the proposed deep-learning framework was a potential method for the characterization of the dry shrinkage behaviors of CEACs.

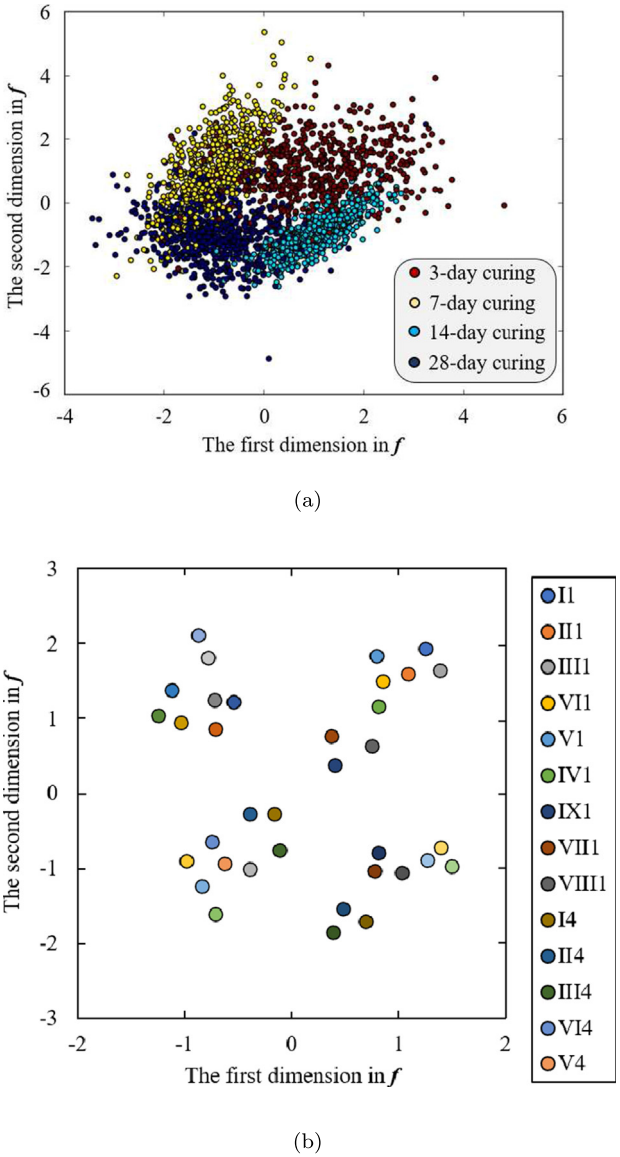

Fig. 9. A t-distributed stochastic neighbor embedding analysis for characterization of dry shrinkage behaviors: (a) training database and (b) testing experiments.

5. Conclusions

In this work, we characterize the hydration and the dry shrinkage behavior of CEACs by a deep-learning framework. The following conclusion can be drawn:

- The main contribution of this work was proposed a deep-learning framework, which had the capacity of characterizing the hydration and the dry shrinkage behavior of CEACs using their design parameters. The framework consisted of GANs and DNNs. The GAN part mapped the design parameters of a CEAC to its XRD spectrum and SEM images, while the DNN part predicted the dry shrinkage ratio of the CEAC based on its design parameters and the outputs of the GAN part. In addition, the feature vector $\boldsymbol{f}$ in the DNN provided a novel method to characterize the effects of the design parameters on the dry shrinkage ratio of the CEAC.
- The GAN part achieved a 0.001 average Euclidean distance between the synthetic and real XDR spectrums, indicating that the two types of the spectrums were highly close. The synthetic XDR spectrums of the testing groups measured the crystallization produces of cement hydration production and calcium hydroxide (portlandite). The synthetic SEM images had the capacity of characterizing the microstructure of CEACs, such as cement hydrates, asphalt, and pore. Therefore, the synthetic

data had the potential of characterizing the hydration processes and the microstructure of CEACs without X-ray diffractometers and an SEMs.

- The DNN part predicted the dry shrinkage ratios of the 36 groups with a 2.70% average error and a 4.29% maximum error. It demonstrated the high and stable precision of the DNN part. The use of the predicted dry ratios qualitatively measured the effects of the design parameters on the dry shrinkage behaviors. The dry shrinkage ratio decreased with the increase of the cement and water contents. Besides, emulsified asphalt had negative effects on the dry shrinkage behavior of the CEACs because of the space-charge effects between cement and emulsified asphalt. In addition, the effects of other factors (e.g., aggregate grading and curing condition) were also characterized by the predicted dry shrinkage ratios.
- The feature vector $\boldsymbol{f}$ in the DNN provided a novel method to quantificationally characterize the effects of the design parameters on the dry shrinkage ratios. From the distribution of $\boldsymbol{f}$ in a two-dimension space, we found that the curing time had the most significant effects on the dry shrinkage ratios, followed by the aggregate grading and the contents of cement and emulsified asphalt. The curing time mainly influenced the hydration processes, while the aggregate grading directly influenced the porosity of the composites. The influence of other factors was also reflected using $\boldsymbol{f}$ in the t-SNE two-dimension space

Declaration of Competing Interest

The authors declare that they have no known competing financial interests or personal relationships that could have appeared to influence the work reported in this paper.

Acknowledgement

This work is supported by Science and Technology Development Project of Xinjiang Production and Construction Corps (No. 2019AB013), Key Research and Development Program of Shaanxi Province of China (No. 2019GY-174), Henan Transportation Science and Technology Plan Project (No. 2019J1), and Project for High Level Talents in Henan Province (No. 204200510004), and Opening Foundation of Research and Development Center of Transport Industry of Technologies, Materials and Equipments of Highway Construction and Maintenance. (Gansu Road & Bridge Construction Group) (No. GLKF201806). This work is also supported by Research and Development Center of Transport Industry of Technologies, Materials and Equipment of Highway Construction and Maintenance (No. 2019–004).

References

[1] J. Yan, Z. Leng, F. Li, H. Zhu, S. Bao, Early-age strength and long-term performance of asphalt emulsion cold recycled mixes with various cement contents, Constr. Build. Mater. 137 (2017) 153–159, https://doi.org/10.1016/j.conbuildmat.2017.01.114.
[2] Y. Wang, Z. Leng, X. Li, C. Hu, Cold recycling of reclaimed asphalt pavement towards improved engineering performance, J. Cleaner Prod. 171 (2018) 1031–1038, https://doi.org/10.1016/j.jclepro.2017.10.132.
[3] Z. Wang, P. Wang, H. Guo, X. Wang, G. Li, Adhesion improvement between rap and emulsified asphalt by modifying the surface characteristics of rap, Adv. Mater. Sci. Eng. (2020).
[4] Y. Zhang, X. Kong, S. Hou, Y. Liu, S. Han, Study on the rheological properties of fresh cement asphalt paste, Constr. Build. Mater. 27 (1) (2012) 534–544, https://doi.org/10.1016/j.conbuildmat.2011.07.010.
[5] Z. Wang, A. Sha, Micro hardness of interface between cement asphalt emulsion mastics and aggregates, Mater. Struct. 43 (4) (2010) 453–461, https://doi.org/10.1617/s11527-009-9502-2.
[6] J. Peng, D. Deng, Q. Yuan, Z. Liu, L. Fang, Study of the rheological behavior of fresh cement emulsified asphalt paste, Constr. Build. Mater. 66 (2014) 348–355, https://doi.org/10.1016/j.conbuildmat.2014.05.023.
[7] S. Oruc, F. Celik, M.V. Akpinar, Effect of cement on emulsified asphalt mixtures, J. Mater. Eng. Perform. 16 (5) (2007) 578–583.
[8] Y. Kim, S. Im, H. Lee, Impacts of curing time and moisture content on engineering properties of cold in-place recycling mixtures using foamed or emulsified asphalt, J. Mater. Civil Eng. 23 (5) (2011) 542–553, https://doi.org/10.1061/(ASCE)MT.1943-5533.0000209.
[9] Z. Wang, Q. Wang, T. Ai, Comparative study on effects of binders and curing ages on properties of cement emulsified asphalt mixture using gray correlation entropy analysis, Constr. Build. Mater. 54 (2014) 615–622, https://doi.org/10.1016/j.conbuildmat.2013.12.093.
[10] Z. Wang, N. Dai, X. Wang, J. Zhang, H. Guo, Laboratory investigation on effects of microwave heating on early strength of cement bitumen emulsion mixture, Constr. Build. Mater. 236 (2020), https://doi.org/10.1016/j.conbuildmat.2019.117439 117439.
[11] Z. Wang, N. Dai, X. Wang, G. Li, H. Guo, Early-stage road property improvements of cold recycled asphalt emulsion mixture with microwave technology, J. Cleaner Prod. 263 (2020), https://doi.org/10.1016/j.jclepro.2020.121451 121451.
[12] W. Fedrigo, W.P. Núñez, T.R. Kleinert, M.F. Matuella, J.A.P. Ceratti, Strength, shrinkage, erodibility and capillary flow characteristics of cement-treated recycled pavement materials, Int. J. Pave. Res. Technol. 10 (5) (2017) 393–402, https://doi.org/10.1016/j.ijprt.2017.06.001.
[13] B. Kiani, A.H. Gandomi, S. Sajedi, R.Y. Liang, New formulation of compressive strength of preformed-foam cellular concrete: an evolutionary approach, J. Mater. Civil Eng. 28 (10) (2016) 04016092.
[14] Y. Tian, D. Lu, R. Ma, J. Zhang, W. Li, X. Yan, Effects of cement contents on the performance of cement asphalt emulsion mixtures with rapidly developed early-age strength, Constr. Build. Mater. 244 (2020), https://doi.org/10.1016/j.conbuildmat.2020.118365 118365.
[15] J. Ouyang, W. Yang, J. Chen, B. Han, Effect of superplasticizer and wetting agent on pavement properties of cold recycled mixture with bitumen emulsion and cement, J. Mater. Civil Eng. 32 (6) (2020) 04020136, https://doi.org/10.1061/(ASCE)MT.1943-5533.0003194.
[16] Y. Liu, Z. Zhang, L. Tan, Y. Xu, C. Wang, P. Liu, H. Yu, M. Oeser, Laboratory evaluation of emulsified asphalt reinforced with glass fiber treated with different methods, J. Cleaner Prod. 274 (2020) 123116.
[17] Z. Zhang, J. Li, Z. Wang, S. Long, S. Jiang, G. Liu, Preparation and performance characterization of a novel high-performance epoxy resin modified reactive liquid asphalt, Constr. Build. Mater. 263 (2020), https://doi.org/10.1016/j.conbuildmat.2020.120113 120113.
[18] Z. Wang, L. Cai, X. Wang, C. Xu, B. Yang, J. Xiao, Fatigue performance of different thickness structure combinations of hot mix asphalt and cement emulsified asphalt mixtures, Materials 11 (7). doi:10.3390/ma11071145..
[19] Y. Yang, S. Dong, Y. Yang, The prediction model of cold recycled materials mechanical properties based on the grey neural network, DEStech Trans. Mater. Sci. Eng. (ICTIM)..
[20] N. Zavrtanik, J. Prosen, M. Tušar, G. Turk, The use of artificial neural networks for modeling air void content in aggregate mixture, Autom. Constr. 63 (2016) 155–161, https://doi.org/10.1016/j.autcon.2015.12.009.
[21] T.B. Moghaddam, M. Soltani, H.S. Shahraki, S. Shamshirband, N.B.M. Noor, M.R. Karim, The use of SVM-FFA in estimating fatigue life of polyethylene terephthalate modified asphalt mixtures, Measurement 90 (2016) 526–533, https://doi.org/10.1016/j.measurement.2016.05.004.
[22] S. Mirabdolazimi, G. Shafabakhsh, Rutting depth prediction of hot mix asphalts modified with forta fiber using artificial neural networks and genetic programming technique, Constr. Build. Mater. 148 (2017) 666–674, https://doi.org/10.1016/j.conbuildmat.2017.05.088.
[23] E.M. Golafshani, A. Behnood, Application of soft computing methods for predicting the elastic modulus of recycled aggregate concrete, J. Cleaner Prod. 176 (2018) 1163–1176, https://doi.org/10.1016/j.jclepro.2017.11.186.
[24] H. Majidifard, B. Jahangiri, W.G. Buttlar, A.H. Alavi, New machine learning-based prediction models for fracture energy of asphalt mixtures, Measurement 135 (2019) 438–451, https://doi.org/10.1016/j.measurement.2018.11.081.
[25] Z. Tong, J. Gao, H. Zhang, Recognition, location, measurement, and 3d reconstruction of concealed cracks using convolutional neural networks, Constr. Build. Mater. 146 (2017) 775–787, https://doi.org/10.1016/j.conbuildmat.2017.04.097.
[26] Z. Tong, J. Gao, A. Sha, L. Hu, S. Li, Convolutional neural network for asphalt pavement surface texture analysis, Comput.-Aided Civil Infrastruct. Eng. 33 (12) (2018) 1056–1072, https://doi.org/10.1111/mice.12406.
[27] Y. Wu, M. Schuster, Z. Chen, Q.V. Le, M. Norouzi, W. Macherey, M. Krikun, Y. Cao, Q. Gao, K. Macherey, J. Klingner, A. Shah, M. Johnson, X. Liu, L. Kaiser, S. Gouws, Y. Kato, T. Kudo, H. Kazawa, K. Stevens, G. Kurian, N. Patil, W. Wang, C. Young, J. Smith, J. Riesa, A. Rudnick, O. Vinyals, G. Corrado, M. Hughes, J. Dean, Google's neural machine translation system: Bridging the gap between human and machine translation, CoRR abs/1609.08144. arXiv:1609.08144..
[28] Y. Zhang, M. Pezeshki, P. Brakel, S. Zhang, C. Laurent, Y. Bengio, A.C. Courville, Towards end-to-end speech recognition with deep convolutional neural networks, CoRR abs/1701.02720. arXiv:1701.02720..
[29] T. Xu, P. Zhang, Q. Huang, H. Zhang, Z. Gan, X. Huang, X. He, Attngan: Fine-grained text to image generation with attentional generative adversarial networks, in: The IEEE Conference on Computer Vision and Pattern Recognition (CVPR), 2018..
[30] J. Gilmer, S.S. Schoenholz, P.F. Riley, O. Vinyals, G.E. Dahl, Neural message passing for quantum chemistry, in: Proceedings of the 34th International Conference on Machine Learning – Volume 70, 2017, pp. 1263–1272..

[31] J.M. Stokes, K. Yang, K. Swanson, W. Jin, A. Cubillos-Ruiz, N.M. Donghia, C.R. MacNair, S. French, L.A. Carfrae, Z. Bloom-Ackerman, V.M. Tran, A. Chiappino-Pepe, A.H. Badran, I.W. Andrews, E.J. Chory, G.M. Church, E.D. Brown, T.S. Jaakkola, R. Barzilay, J.J. Collins, A deep learning approach to antibiotic discovery, Cell 180 (4) (2020) 688–702.e13, https://doi.org/10.1016/j.cell.2020.01.021.
[32] J. Xiao, W. Jiang, W. Ye, J. Shan, Z. Wang, Effect of cement and emulsified asphalt contents on the performance of cement-emulsified asphalt mixture, Constr. Build. Mater. 220 (2019) 577–586, https://doi.org/10.1016/j.conbuildmat.2019.06.051.
[33] O. Xu, Z. Wang, R. Wang, Effects of aggregate gradations and binder contents on engineering properties of cement emulsified asphalt mixtures, Constr. Build. Mater. 135 (2017) 632–640, https://doi.org/10.1016/j.conbuildmat.2016.12.095.
[34] W. Dong, L. Xie, P. Pan, A comparative study on early-stage strength development and mechanical properties of cement emulsified asphalt mixture using brake pad waste, Constr. Build. Mater. 184 (2018) 515–523, https://doi.org/10.1016/j.conbuildmat.2018.07.013.
[35] H. Liu, A. Sha, Z. Tong, J. Gao, Autonomous microscopic bunch inspection using region-based deep learning for evaluating graphite powder dispersion, Constr. Build. Mater. 173 (2018) 525–539, https://doi.org/10.1016/j.conbuildmat.2018.04.050.
[36] Z. Tong, H. Guo, J. Gao, Z. Wang, A novel method for multi-scale carbon fiber distribution characterization in cement-based composites, Constr. Build. Mater. 218 (2019) 40–52, https://doi.org/10.1016/j.conbuildmat.2019.05.115.
[37] Z. Tong, J. Gao, Z. Wang, Y. Wei, H. Dou, A new method for CF morphology distribution evaluation and CFRC property prediction using cascade deep learning, Constr. Build. Mater. 222 (2019) 829–838, https://doi.org/10.1016/j.conbuildmat.2019.06.160.
[38] D. Yuan, W. Jiang, Z. Tong, J. Gao, J. Xiao, W. Ye, Prediction of electrical conductivity of fiber-reinforced cement-based composites by deep neural networks, Materials 12 (23). doi:10.3390/ma12233868..
[39] Z. Tong, J. Huo, Z. Wang, High-throughput design of fiber reinforced cement-based composites using deep learning, Cem. Concr. Compos. 113 (2020), https://doi.org/10.1016/j.cemconcomp.2020.103716 103716.
[40] Y. Yu, Z. Gong, P. Zhong, J. Shan, Unsupervised representation learning with deep convolutional neural network for remote sensing images, in: Image and Graphics, Cham, 2017, pp. 97–108. doi:10.1007/978-3-319-71589-6_9.
[41] S. Reed, Z. Akata, X. Yan, L. Logeswaran, B. Schiele, H. Lee, Generative adversarial text to image synthesis, in: Proceedings of The 33rd International Conference on Machine Learning, Vol. 48 of Proceedings of Machine Learning Research, PMLR, New York, USA, 2016, pp. 1060–1069. http://proceedings.mlr.press/v48/reed16.html.
[42] B. Shao, Q. Li, X. Jiang, A survey of dcgan based unsupervised decoding and image generation, Int. J. Comput. Appl. 975 8887. doi:10.5120/ijca2019919099..
[43] Z. Tong, D. Yuan, J. Gao, Z. Wang, Pavement defect detection with fully convolutional network and an uncertainty framework, Comput.-Aided Civil Infrastruct. Eng. n/a (n/a). doi:10.1111/mice.12533..
[44] S. Ioffe, C. Szegedy, Batch normalization: Accelerating deep network training by reducing internal covariate shift, CoRR abs/1502.03167. arXiv:1502.03167..
[45] Y. LeCun, Y. Bengio, G. Hinton, Deep learning, Nature 521 (7553) (2015) 436–444. doi:10.1038/nature14539..
[46] Z. Tong, J. Gao, D. Yuan, Advances of deep learning applications in ground-penetrating radar: a survey, Constr. Build. Mater. 258 (2020), https://doi.org/10.1016/j.conbuildmat.2020.120371 120371.
[47] Z. Tong, J. Gao, Z. Han, Z. Wang, Recognition of asphalt pavement crack length using deep convolutional neural networks, Road Mater. Pave. Design 19 (6) (2018) 1334–1349, https://doi.org/10.1080/14680629.2017.1308265.
[48] Z. Tong, J. Gao, H. Zhang, Innovation for evaluating aggregate angularity based upon 3d convolutional neural network, Constr. Build. Mater. 155 (2017) 919–929, https://doi.org/10.1016/j.conbuildmat.2017.08.129.
[49] Z. Tong, D. Yuan, J. Gao, Y. Wei, H. Dou, Pavement-distress detection using ground-penetrating radar and network in networks, Constr. Build. Mater. 233 (2020), https://doi.org/10.1016/j.conbuildmat.2019.117352 117352.
[50] Z. Tong, J. Gao, H. Zhang, Innovative method for recognizing subgrade defects based on a convolutional neural network, Constr. Build. Mater. 169 (2018) 69–82, https://doi.org/10.1016/j.conbuildmat.2018.02.081.
[51] I. Goodfellow, J. Pouget-Abadie, M. Mirza, B. Xu, D. Warde-Farley, S. Ozair, A. Courville, Y. Bengio, Generative adversarial nets, in: Advances in Neural Information Processing Systems, 2014, pp. 2672–2680..
[52] T. Fawcett, An introduction to roc analysis, Pattern Recogn. Lett. 27 (8) (2006) 861–874, https://doi.org/10.1016/j.patrec.2005.10.010.
[53] L. v. d. Maaten, G. Hinton, Visualizing data using t-SNE, J. Mach. Learn. Res. 9 (Nov) (2008) 2579–2605..